machines

MDPI

Article

Speed Control with Indirect Field Orientation for Low Power Three-Phase Induction Machine with Squirrel Cage Rotor

Robert R. Gomes *, Luiz F. Pugliese, Waner W. A. G. Silva, Clodualdo V. Sousa, Guilherme M. Rezende and Fadul F. Rodor

Institute of Technological Sciences, Federal University of Itajubá, Itabira 35903-087, Brazil; pugliese@unifei.edu.br (L.F.P.); waner@unifei.edu.br (W.W.A.G.S.); clodualdosousa@unifei.edu.br (C.V.S.); guilhermemre@unifei.edu.br (G.M.R.); fadulrodor@unifei.edu.br (F.F.R.)

* Correspondence: robertribeiro@unifei.edu.br; Tel.: +55-(31)-98815-1828

Abstract: Induction machines are widely used in the industry due to their many advantages compared to other industrial machines. This article presents the study and implementation of speed control applied to a Three-phase Induction Machine (MIT) of the squirrel cage type. The induction motor was modeled using the rotor flux in the synchronous reference to design Proportional-Integral (PI) type controllers for the current and velocity control loops. It is the objective of the article also to present in detail the development of converter hardware that comprises the stages of power, acquisition, and conditioning of engine signals. The system was simulated using computational tools and validated using a prototype designed, constructed, and commissioned.

Keywords: induction machines; electrical machines; vector control; SVPWM modulation; frequency inverter

Citation: Gomes, R.R.; Pugliese, L.F.; Silva, W.W.A.G.; Sousa, C.V.; Rezende, G.M.; Rodor, F.F. Speed Control with Indirect Field Orientation for Low Power Three-Phase Induction Machine with Squirrel Cage Rotor. *Machines* **2021**, *9*, 320. https://doi.org/10.3390/machines9120320

Academic Editor: Marcos de Sales Guerra Tsuzuki, Marcosiris Amorim de Oliveira Pessoa and Alexandre Acássio

Received: 27 October 2021
Accepted: 23 November 2021
Published: 27 November 2021

1. Introduction

Electrical machines play an essential role in the industry and the development of society, they make up an efficient means of electromechanical conversion. The industrial modernization process increasingly requires the application of electric motors in drive systems, which often requires control of torque, acceleration, speed or position.

Variable speed drives are mainly used in applications, such as electrical vehicles, pumps, elevators, fans, ventilation, heating, robotics, ship propulsion, and air conditioning [1–3]. The benefits of squirrel-cage induction motors—high robustness and low maintenance—make it widely used through various industrial modern processes, with growing economical and performing demands [1,4].

Previously, the use of motors in industrial applications that required good performance in position and speed control were limited to DC machines. Such use was due to the inherent decoupling characteristics of the machine: one electrical circuit to impose magnetic flux on the machine (field) and another to impose torque (power), which simplifies the control of torque, position, and speed of the machine [5].

The advancement of power electronics, control theory, growth of studies in the field of microelectronics and the advancement of digital processor technology, allowed the efficient use of the electric motor in the activation of the most varied industrial loads, enabling the use of alternating current machines in applications of high dynamic performance [6,7].

Thus, the alternating current motor has become widely used in the industry since it presents characteristics such as robustness, low manufacturing cost, absence of sliding contacts and possibility of operating a wide range of torque and speed [8].

The scalar control technique is simple to implement. Although the constant voltage/frequency control method is the simplest, the performance of this method is not good enough [9–11]. Vector-based control methods enable the control of voltage and frequency

amplitude unlike the scalar method. They also provide the instantaneous position of the current, voltage and flux vectors [12].

The dynamic behavior of the IM drives is also improved significantly using the vector-based control method. However, the existence of the coupling between the electromagnetic torque and the flux increases the complexity of the control. To deal with this inherent disadvantage, several methods have been proposed for the decoupling of the torque and flux.

One difficulty of its use for position or speed control is its complex mathematical modeling, requiring greater computational effort for its implementation [5]. In addition, in induction machines there is no unique physical circuit for the field, and this makes its control more complex [13,14].

In Induction Machines (IM), the power phases of the machine each contribute to maintaining the concatenated magnetic flux of the machine and are thus coupled to each other through mutual inductances. To solve the problem of induction machine control, axis transformation techniques are used, which make it possible to transform the electrical and mechanical model of an induction machine so that the flux and torque of the machine can be controlled independently, known as field-oriented control or vector control [15].

The field-oriented control technique is widely used in high-performance motion control applications of induction motors. However, in real applications, accurate decoupling of torque and flux cannot be achieved with accuracy due to the uncertainties of the machine parameters present in the model. These uncertainties are associated with external disturbances, unpredictable parameter variations, and unmodeled nonlinear plant dynamics. Consequently, this deteriorates the dynamic performance of flux and speed significantly. In general, the performance of this technique is dependent on the accuracy of the mathematical model of the induction motor [16].

Field oriented control consists of concentrating the rotor flux on the direct axis of the synchronous reference system, thus achieving decoupling of the flux and torque loops, like DC machines. It is a highly computational technique that involves many mathematical transformations and requires powerful microcontrollers such as Digital Signal Processors (DSPs) and Digital Signal Controllers (DSC) [17].

In general, the field-oriented control performance is sensitive to the deviation of motor parameters, particularly the rotor time constant [7,18,19]. To deal with this problem, there are many fluxes measurement and estimation mechanisms in the published literature [18–21].

Speed information is required for the operation of vector-controlled IM drive. The rotor speed can measure through a mechanical sensor or can be estimated using voltage, current signals, and machine parameters [22,23]. The use of speed sensors is associated with some drawbacks, such as noise present in the measurement, requirement of shaft extension, reduction of mechanical robustness of the motor drive, not suitable for hostile environments and more expensive [24]. On the other hand, using the sensorless strategy reduces hardware complexity, reduces costs, elimination of the sensor cable, better noise immunity, higher reliability, and less maintenance requirements [22].

In this context, the work presents the design and commissioning steps of a three-phase frequency inverter for the activation of a small three-phase induction machine. In addition, the simulation and control of the machine will be addressed through the Indirect Oriented Field Control strategy (IFOC). In this work, the main components that make up the power circuit, current, voltage and speed measurement circuits will be presented. It is also presented the models used for the design of the current and speed controllers of the vector control and, later, the validation in the simulation environment and the experimental bench. In addition, in this work an encoder attached to the machine shaft is used to measure the position and speed of the rotor to prevent parametric variations and speed estimation errors from affecting the quality of the indirect field control. Also, the tests performed in this work are for lower speeds and without a load attached to the machine shaft.

The main contribution of this paper is to propose the design and commissioning of a low-cost converter to drive an induction machine using the indirect field control strategy with a sensor attached to the shaft.

The work is organized as follows: Section 2 will deal with the description of all the hardware used in the construction of the prototype. Section 3 will describe the dynamic modeling of the field oriented directly to the three-phase induction motor. Section 4 will describe the concepts related to Space Vector Pulse Width Modulation (SVPWM). Section 5 will display the tuning of the controllers for the current and speed loops. Section 6 is responsible for presenting the results obtained in the computational simulation as well as the practical tests performed in the prototype developed. Finally, Section 7 presents the conclusions of the work.

2. Hardware Description

The designed converter is based on the FNA41560 IC (Integrated Circuit) produced by Fairchild Semiconductor's. This Insulated Gate Bipolar Transistor (IGBT) module is designed for low-power AC (Alternating Current) motor drive applications, cooler and air conditioning. The device responsible for the data acquisition, processing and execution of the vector control algorithm is the C2000 Delfino MCU TMS320F28379D LaunchPad microprocessor from Texas Instruments.

Figure 1 presents the system built to perform the experimental tests.

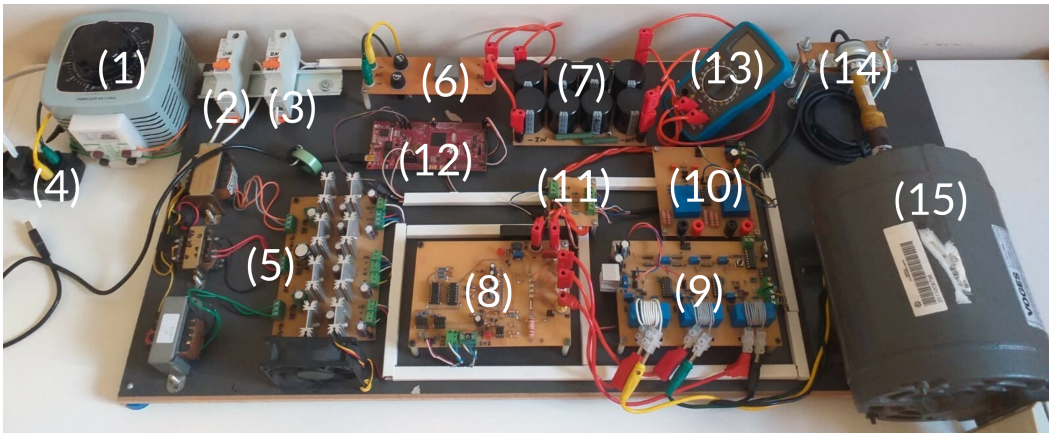

Figure 1. Experimental bench built.

The experimental bench is composed of:

1. Variable auto transformer;
2. Auxiliary source power supply circuit breaker;
3. Circuit breaker of the capacitor bank pre-charge circuit;
4. AC power input;
5. Auxiliary voltage source;
6. Rectifier circuit;
7. DC link;
8. Three-phase inverter;
9. Current acquisition board;
10. Voltage acquisition board;
11. Encoder signal conditioning board;
12. TMS320F28379D DSP (Digital Signal Processor);
13. Digital multimeter;
14. Incremental encoder;
15. Three-phase induction motor.

There are two basic types of inverters, Voltage Source Inverter (VSI), powered by a voltage source, and Current Source Inverters (CSI) powered by a current source. VSI topology is more common and synthesizes a well-defined voltage in the machine terminals while CSI provides a current signal in the machine terminals [5].

Figure 2 presents the simplified schematic diagram of a VSI. This setting uses a rectifier to transform the AC input signal into DC. After rectification, the signal is filtered by the DC link to obtain a signal without oscillations. Next, the DC signal is applied to the three-phase IGBT bridge with the sole purpose of creating an alternating signal at the output by switching the semiconductor frequently defined by the modulation technique employed.

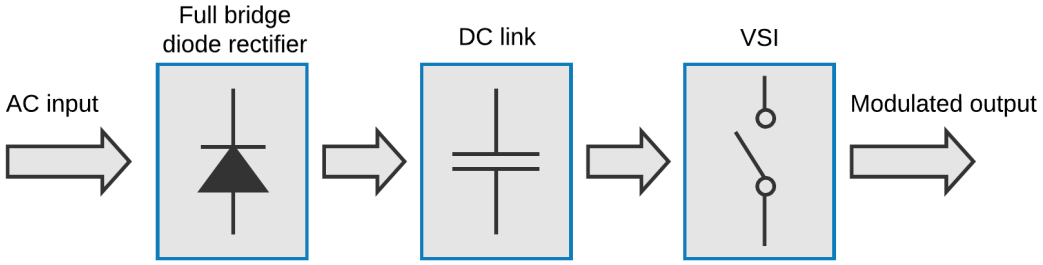

Figure 2. Diagram of a voltage inverter.

2.1. Digital Signal Processor

The TMS320F28379D microcontroller is designed for application in control systems, drive drivers, signal detection and processing. The DSP has two Central Processing Units (CPU), two Control Law Accelerator (CLA) and a maximum adjustable clock of 200 MHz [25,26].

LaunchPad features 32-bit architecture, 1 MB of flash memory, 204 kB of RAM, 14 analog-to-digital conversion channels (ADC) with 16/12-bit resolution and 14 channels designated for PWM function [25,27,28].

2.2. Rectifier

Rectifiers can be classified according to the number of phases of the input AC voltage source, i.e., single-phase or three-phase. Depending on the semiconductors used, they can be classified as uncontrolled, semi-controlled, or fully controlled. Also, concerning topology, they can be classified as half-wave or full-wave rectifiers [29]. The three-phase uncontrolled full-wave rectifier topology is common in converter drive applications because it uses diodes as the rectifying element, connected in a full-bridge arrangement.

In this configuration, the entire cycle of the alternating voltage of the power supply is rectified, providing in the voltage output a constant average value and with smaller oscillations [29]. For this work, the full-wave bridge rectifier configuration encapsulated in the KBPC3510 IC is used. This rectifier allows a maximum current of 10 A, enough to supply the consumption of the three-phase induction motor used.

2.3. DC Link

The design of the DC link capacitors considers the power of the converter load, the maximum permissible voltage variation, and the hold-up time of the load, which is defined as the time that the output voltage should remain constant in the event of a momentary fault in the capacitor bank's input voltage. The Equation (1) is used to design the capacitor bank, given by

$$C_o = \frac{2P_{rated}t_H}{0.19V_{rated}^2} \quad (1)$$

where P_{rated}, t_H, V_{rated} represent the rated power, hold-up time, and rated feed voltage of the machine, respectively. The variation of the output voltage was defined at 10% and the hold-up time of 8.33 ms, that is, a half cycle of the nominal frequency of the load. Thus, the capacitance value of the projected DC link is 4.4 mF, in which a total of eight EPCOS

B43845 capacitors of 2200 µF and voltage of 200 V_{dc} were used. The designed DC link can work with voltages up to 400 V_{dc}, enabling AC voltage connection at the rectifier input of 127 V_{rms} or 220 V_{rms}.

The DC link also contains pre-charge and bank discharge resistors. The pre-charge resistor is responsible for preventing a high in-rush current from flowing through the converter elements and damaging the components when the rectifier's AC supply circuit breaker is tripped. The single-phase variable autotransformer at the input of the rectifier circuit was also employed for this purpose, allowing the input AC voltage to rise gradually to the value of 220 V_{rms}.

The discharge resistor has the function of draining the energy stored in the capacitors when the converter is switched off, ensuring that the voltage reduces to zero slowly, also avoiding accidents. Another function of the discharge resistor is to work as a braking resistor when the machine starts to work as a generator due to the type of load it drives. In this context, the DC link voltage tends to rise due to the reverse power flow. Figure 3 illustrates the simplified DC link circuit with the pre-charge (R_{pc}) and discharge (R_d) resistors.

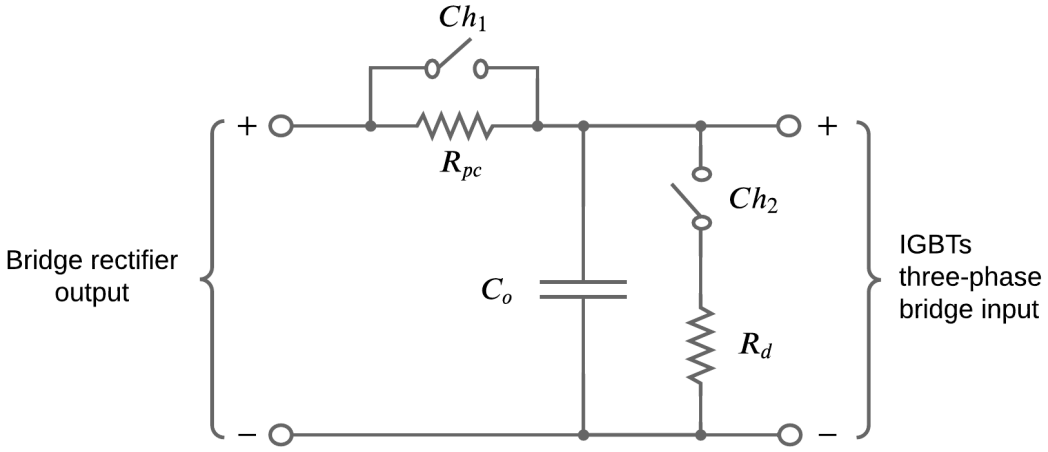

Figure 3. DC link with pre-charge and discharge resistors [30].

The AC voltage at the input of the rectifier circuit is 220 V_{rms}. Thus, the DC voltage at the output of the rectifier corresponds to the maximum value of the input voltage, i.e., 311 V_{dc}. The pre-charge resistor was chosen so that the link voltage reaches the maximum value (311 V_{dc}) in 5 s, while the discharge resistor was chosen so that the bank voltage is zero in 132 s. The Ch_1 switch is open only at the beginning of bank charging, and after the bank voltage stabilizes the switch is closed since the pre-charge resistor is no longer needed. Similarly, the switch (Ch_2) is closed when the converter is switched off, allowing the stored energy in the bank to be drained, and when in the normal operation of the converter, Ch_2 is open.

2.4. Power Module

The choice of Fairchild Semiconductor's FNA41560 driver is a consequence of the need for a compact and high-performance solution for the frequency inverter. The chip features optimized circuit protection and a combined IGBT drive to reduce losses. The module is also equipped with overcurrent protection, under-voltage interlocks, temperature monitoring output, bootstrap diodes and features gate drive circuits and internal dead-time.

The FNA41560 must be powered with a voltage of 15 V_{dc}, supports 600 V_{dc} (drain-source voltage) in the IGBT while dissipating 41 W of power in each semiconductor. The module operates with a maximum switching frequency of 20 kHz, a maximum current of 15 A at 25 °C, an insulation rating of 2000 V_{rms}/min and terminals for individual current monitoring of each phase [31].

The power module has six PWM outputs to drive the IGBTs, which can be controlled by the DSP via optocoupler ICs. The PWM modules of the DSP have complementary

outputs and internal dead-time production. However, a gate drive circuit was designed to receive the command signals from the upper switches of the three-phase IGBT bridge and, from these, the command signals of the lower switches and the dead-time between the switches of the same arm are produced via hardware. In this way, configuration errors of the PWM channels and dead-time of the DSP that could damage the FNA41560 are avoided. Figure 4 illustrates the dead-time generation circuit for the U-arm of the three-phase IGBT bridge.

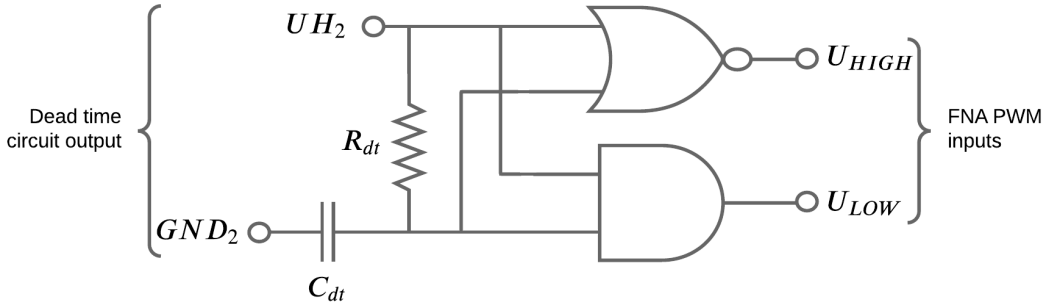

Figure 4. Circuit to generate the complementary PWM and dead-time signals [30].

From Figure 4 it is noted that the circuit to generate the complementary signals has a resistor (R_{dt}) and a capacitor (C_{dt}) to generate the dead-time between the switches of the same arm along with AND and NOR logic gates. The switching frequency chosen is 10 kHz, within the operating range of the FNA41560. Thus, the resistor and capacitor were set to guarantee a dead-time of 1 µs equivalent to 1% of the switching period.

The designed PCB of the IGBT module contains three dead-time generation circuits and complementary signals. Looking at Figure 4, when applying a high logic level signal to the UH_2 input of the first arm, the U_{HIGH} output also assumes high logic level. However, the U_{LOW} output, which drives the lower IGBT, has a low logic level with the addition of the time delay, preventing simultaneous driving of the switches. The same principle is extended to the switches of the V and W arms of the three-phase IGBT bridge.

In addition, to drive the module's switches, optical isolation circuits or optocoupler circuits were used. These are circuits used with the purpose of electrical decoupling, the PWM channels of the DSP do not have a direct electrical connection with the inputs of the FNA41560. Its working principle is based on a Light Emitting Diode (LED) that, when energized, emits a light that puts a phototransistor in a conduction state [32].

The necessity for electrical isolation comes from the fact that there are voltages and currents in the power stage that could cause damage to the control and data acquisition circuits. For this reason, the reference of the power module is different from the reference of the DSP and the data acquisition boards, ensuring the isolation of the control and measurement circuits from the power circuits.

For this project, it was chosen to use optocouplers of the HCPL2630 type. These ICs work with Transistor-Transistor Logic (TTL) logic level, considerable electrical isolation, 12 ns delay time and have two independent channels in the same encapsulation [33].

Figure 5 illustrates the circuit developed to isolate PWM signals from the DSP to the FNA41560 driver.

The PWM signals coming from the DSP have as reference GND_1, while at the output of the optocouplers (power stage), the reference is GND_2. At the output of the isolation circuit, the PWM signals are injected into the dead-time circuits and there is the generation of the complementary PWM to drive the IGBTs of the power module.

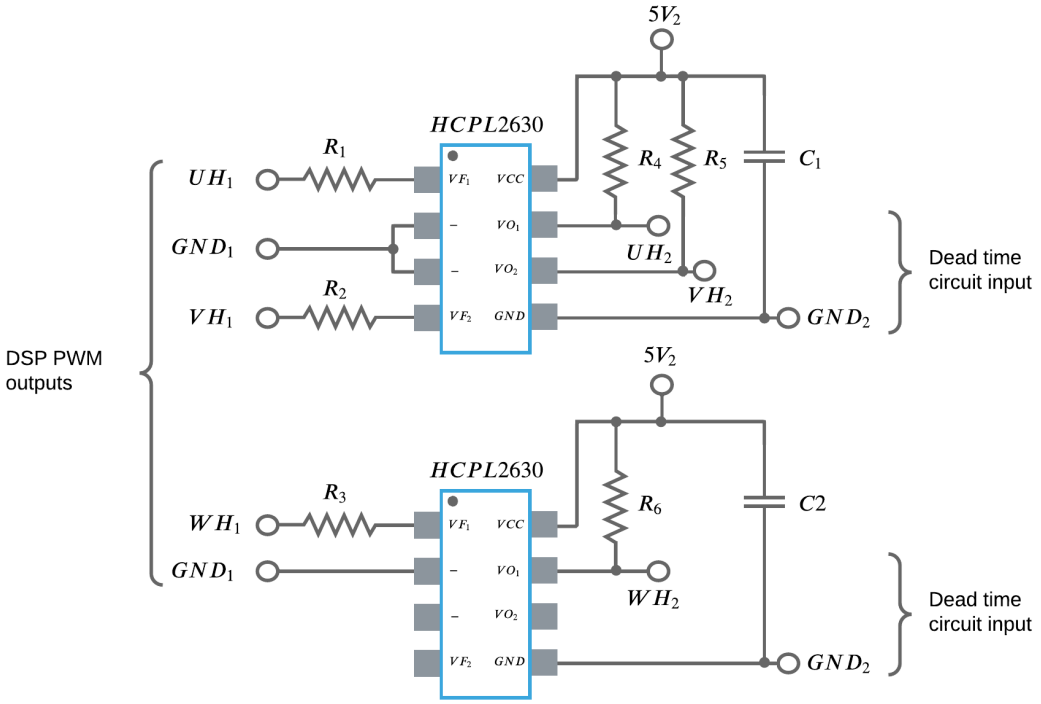

Figure 5. PWM signal isolation circuit [30].

To monitor the temperature of the power module, a voltage comparator circuit with a variable resistor was designed to adjust the maximum temperature limit of the FNA41560. The IGBT module has an internal thermistor that changes its resistance according to the temperature change. If the module temperature exceeds the set limit, the circuit containing the operational amplifier LM2904 changes the state of the output from logic level low to high. In this context, the signal at a logic high level triggers an LED as a visual alert, in addition to sending a pulse to the DSP to interrupt the PWM signals from the IGBTs.

Figure 6 presents the circuit used for under-voltage blocking recommended by the FNA41560 manufacturer. Also, a 4N25 optocoupler and a voltage divider circuit were used to transmit the signal to the DSP.

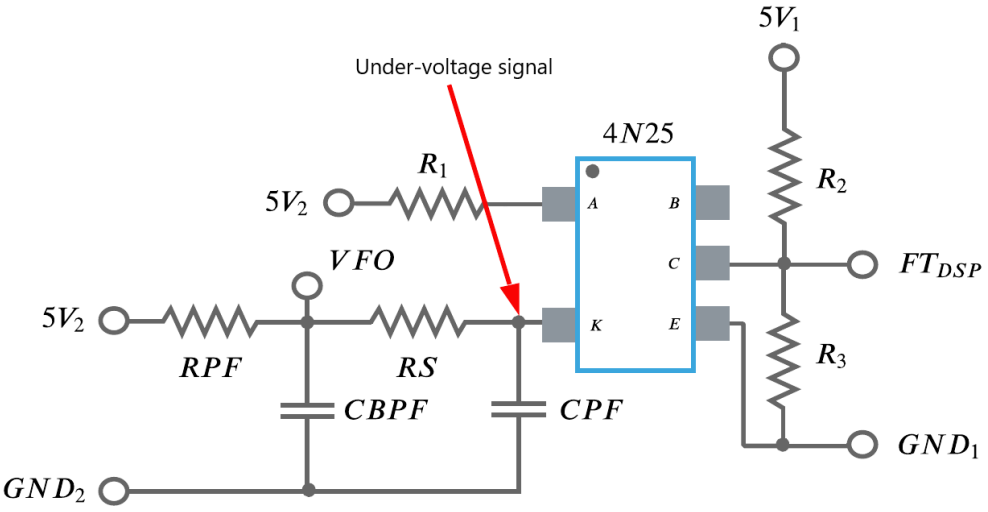

Figure 6. FNA41560 under-voltage detection circuit [30].

The resistors RPF, RS and the capacitors CPF, CBPF are defined according to the module datasheet. The resistor R_1 is used to limit the current of the optocoupler LED, the resistors R_2 and R_3 are the voltage divider resistors. The values of 200 Ω, 10 kΩ and 20 kΩ respectively

have been set. The terminals "A" and "K" of the 4N24 IC indicate the Anode and Cathode terminals of the LED. The terminals "C", "B" and "E" represents the collector, base and emitter terminals of the phototransistor, respectively.

Short-circuit current detection of the FNA41560 is provided by a shunt resistor located at the source terminals of the lower IGBTs of the three-phase bridge. If the voltage across the resistor exceeds the short-circuit threshold voltage trip level (0.5 V_{dc}) at the C_{sc} input of the module, a fault signal is assigned and the lower arm IGBTs are turned off [34].

The protection circuit contains a low-pass filter, formed by resistors R_f and capacitor C_{sc}. The module manufacturer suggests values for these components in such a way that the time constant is between 1 µs and 2 µs. A 15 Ω resistor and 100 nF capacitor were used, i.e., filter time constant of 1.5 µs. A shunt resistor with a value of 0.1 Ω was sized. Thus, for the protection to operate, a current greater than or equal to 5 A circulating through the module is required.

2.5. Current Measurement

The current measurement of the converter was made using the LA 55-P Hall-effect sensor from the LEM manufacturer. Table 1 presents the characteristics of the transducer.

Table 1. LA 55-P sensor characteristics [35].

Electrical Data	Value
Primary nominal R.M.S current	50 A
Secondary nominal R.M.S current	50 mA
Conversion ratio	1:1000
Supply voltage	±12 or 15 V

When an electrical current circulates through the primary winding (I_p) of the current sensor, a current also circulates in the secondary (I_s) proportional to the conversion ratio of the transducer. The current in the secondary in turn produces a voltage (V_{in}) on the shunt resistor R_m and thus this voltage signal is fed into the non-inverting adder circuit. In the design of the current acquisition circuit, it was chosen to use the TL084 operational amplifier and the R_m resistor was set to a value of 100 Ω. The current conditioning circuit is shown in Figure 7.

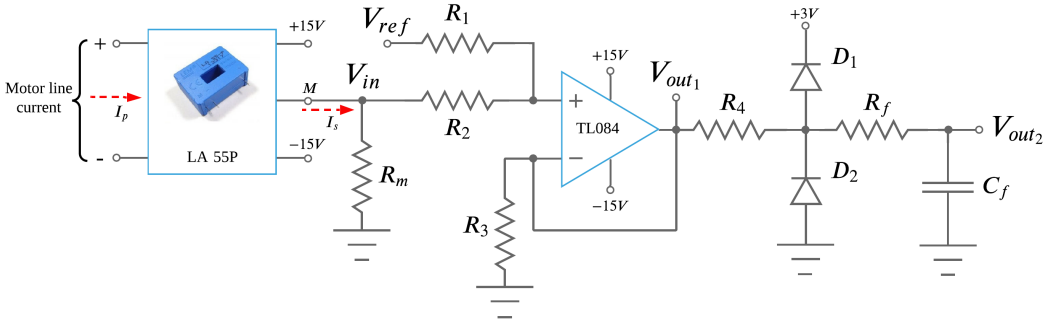

Figure 7. Current signal conditioning circuit.

The voltage signal V_{ref} is responsible for adding an offset voltage to the signal. Since the analog-to-digital conversion channels of the DSP operate with input voltages between 0 and 3 V_{dc}, an offset voltage must be added to the input signal such that this voltage represents the null measurements of the sensor, while voltages above the offset value represent positive measurements of the sensor and voltages below the offset voltage represent negative measurements. The Equation (2) presents the relationship between output voltage V_{out1} with inputs V_{ref} and V_{in}, given by

$$V_{out1} = \frac{V_{in}}{2} + \frac{V_{ref}}{2} \quad (2)$$

Therefore, the output voltage is given by half of the reference voltage and half of the input voltage. The output signal of the non-inverting adder circuit passes through a clipper circuit, composed of two diodes and a resistor, whose function is to limit the output voltage of the operational amplifier between 0 and 3 V_{dc}.

A simulation was developed to evaluate the operation of the current conditioning circuit. Considering a current in the secondary of the transducer of 10 mA and reference voltage of 3 V_{dc}, i.e., offset voltage of 1.65 V_{dc} to ensure that the post-processing signal remains in the middle of the reading range. In addition, a signal with a frequency of 10 kHz and amplitude of 0.05 V was added to the input signal to represent the noise present in the current measurement as a function of power module switching.

Figure 8 shows the result of the current conditioning circuit simulation.

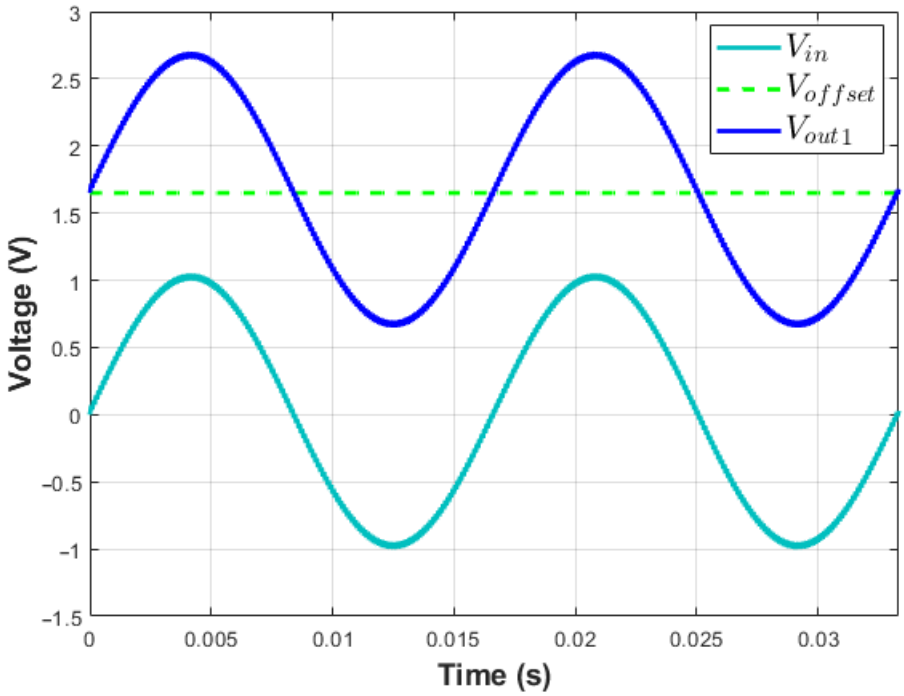

Figure 8. Simulation of the conditioning circuit of the current sensor.

By inspecting Figure 8, it is possible note that the V_{out1} voltage signal oscillates over the offset voltage value and remains between 0 and 3 V_{dc}. However, the voltage signal representing the current is not exclusively sinusoidal, it contains a high-frequency component, coming from the switching of the power module. Thus, it is desirable to remove the ripple caused by switching. The RC loop consisting of R_f and C_f, operating as a passive anti-aliasing low-pass filter was inserted into the output of the conditioning circuit, as presented in Figure 7. The Equation (3) is used to calculate the filter cutoff frequency, given by

$$f_c = \frac{1}{2 \cdot \pi \cdot R_f \cdot C_f} \quad (3)$$

A cutoff frequency of 2.4 kHz was adopted for the filter and, thus, the value of the resistor used was 2 kΩ and the capacitor of 33 nF. Figure 9 shows the comparison between the input voltage signal and the voltage signal after the low-pass filter.

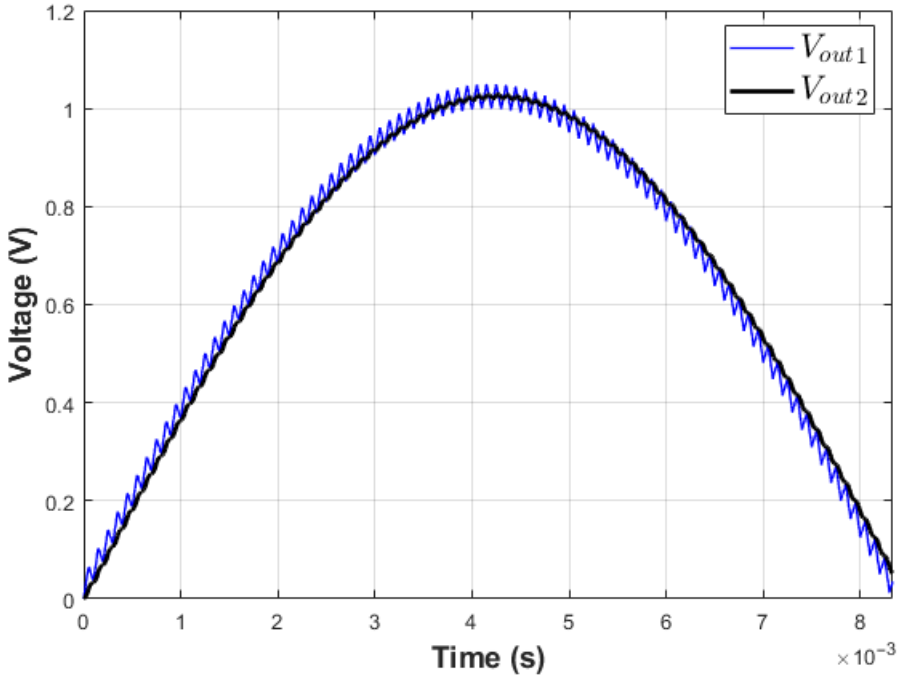

Figure 9. Simulation of the RC anti-aliasing filter.

From Figure 9 it is noted that the ripple caused by switching has been considerably attenuated by the filter used. It can also be seen that a delay has been incorporated into the signal, but not very significantly.

2.6. Voltage Measurement

The LV 20-P voltage transducer from the manufacturer LEM was used for voltage measurement. Table 2 shows the characteristics of the sensor.

Table 2. LV 20-P sensor characteristics [36].

Electrical Data	Value
Measuring nominal voltages	10–500 V
Primary nominal R.M.S current	10 mA
Secondary nominal R.M.S current	25 mA
Conversion ratio	2500:1000
Supply voltage	±12 or 15 V

When applying a voltage to the sensor measuring terminals, a current (I_p) is produced in the primary winding. Thus, in the secondary, the current (I_s) is produced due to the transducer conversion ratio. In turn, the current in the secondary produces a voltage on the shunt resistor (R_m) which reflects the voltage applied to the primary of the sensor.

The voltage conditioning circuit is like the current conditioning circuit, shown in Figure 10.

From Figure 10 it is noted the presence of resistors on the primary side of the voltage sensor. The function of this resistor is to limit the transducer primary current according to the information presented in Table 2. Thus, it was adopted for the R_1 resistor a value of 75 kΩ, enabling the measurement of voltages up to 500 V. For the shunt resistor R_m a value of 100 Ω was adopted.

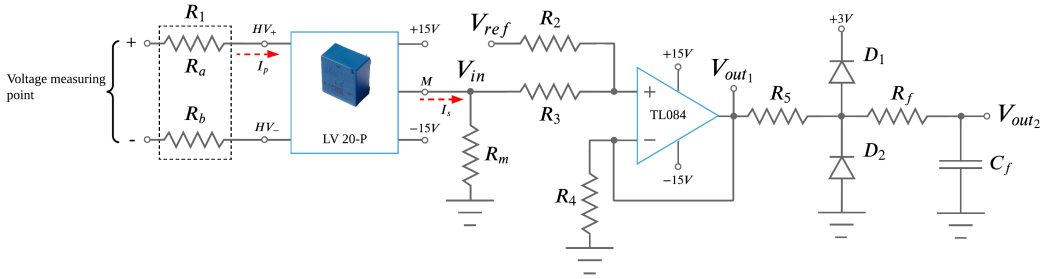

Figure 10. Voltage signal conditioning circuit.

2.7. Measurement of Rotor Position and Speed

The measurement of the machine's speed, position and direction of rotation can be accomplished through the encoder. The encoder used, called incremental with quadrature output, is a device capable of converting shaft rotation information into pulse train signals. State-of-the-art encoders mostly operate on potentiometric, capacitive, magnetic, or optical principles [37].

The incremental encoder is composed of a disk with a series of slots, an infrared light source, and a photoelectric sensor that produce the electrical pulses of channel A. The direction of rotation is obtained by the second strip of slots, channel B, positioned such that they produce an electrical 90° lag concerning channel A. The frequency of the pulse train of channels A and B are directly proportional to the rotational speed of the machine's rotor. The third channel (index) outputs a high logic level signal with each complete revolution of the encoder disk. Figure 11 shows the encoder conditioning circuit and the pulse train of each output channel.

The output voltage of the channels is 12 V_{dc}, as a function of the encoder supply which is 12 V_{dc}. To connect these signals to the DSP's eQEP (Enhanced Quadrature Encoder Pulse) inputs, voltage divider circuits were used to reduce the voltage of the three output channels. In addition, operational amplifiers were used in the voltage buffer configuration, isolating the input signal from the DSP.

The encoder model used for the development of this work is the E30S4 and has an output with a resolution of 360 pulses per revolution.

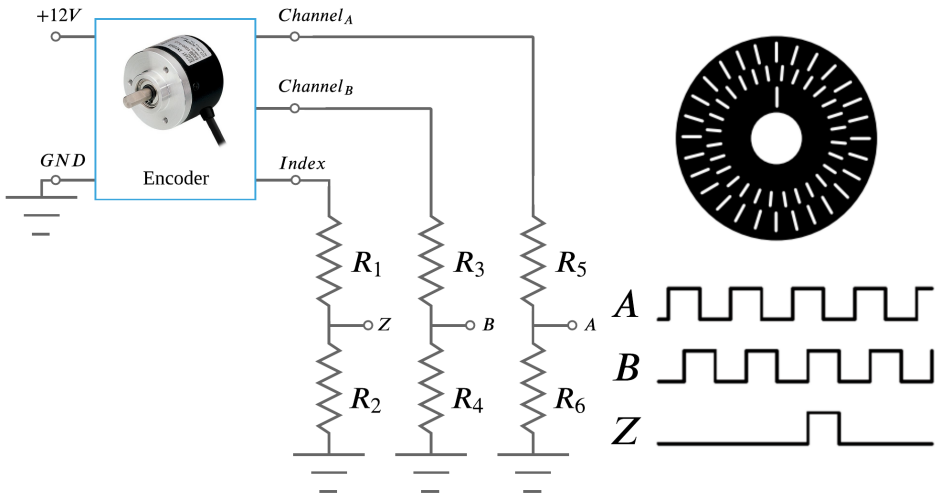

Figure 11. Encoder signal conditioning circuit.

2.8. Auxiliary Voltage Source

The auxiliary voltage source has multiple outputs: ±15 V_{dc}, ±12 V_{dc}, 5 V_{dc} and 3.3 V_{dc}. These voltages are required to power the integrated circuits and sensors of the current measurement boards, voltage measurement, encoder, and complementary power driver circuits. It is also important to mention the need to use voltage sources isolated concerning

the sources that power the power driver, to prevent short circuits in the power step damage the inverter measurement and control circuits.

2.9. Induction Motor Parameters

For the experiments, an induction motor from the manufacturer Voges was used. Table 3 shows the electrical and mechanical parameters of the machine.

Table 3. Parameters of the motor used.

Board Data			
Potency	1 HP	Rotation	1730 RPM
Voltage (Δ)	220 V	I(Δ)	4.0 A
Frequency	60 Hz	Ip/In	5.4
Test Data			
R_s	7.8650 Ω	R_r	4.9925 Ω
L_s	0.1340 H	L_r	0.1340 H
L_m	0.1249 H	σ	0.1312
J	0.0012 kgm^2	B	0.000397 Nms

Some parameters were collected directly from the motor board data and others were obtained through the blocked-rotor and no-load tests.

3. Dynamic Modeling of the Indirect Field Oriented for the MIT

The field-oriented control strategy is classified according to the method of acquisition of the rotor flux angle. In the direct method (Direct Field Oriented Control—DFOC), sensors installed in the machine's air gap are used to measure the flux. In the indirect method (IFOC), there is no flux measurement, the position and slip are used to obtain the position of the rotor flux angle [5].

The IFOC makes use of the fact that satisfying the relationship between slipping and stator current is a necessary and sufficient condition to produce field orientation [5].

In Field Oriented Control (FOC), one can make a direct analogy with the field-independent DC machine control [38]. In DC machines, the magnetic flux established by the armature and field currents is orthogonal to each other, regardless of the rotor's position and mechanical load. Thus, for a constant field current level, the armature current is responsible for the machine's torque production. In asynchronous machine FOC, the same principle applies, where the direct axis current is responsible to establish the machine's magnetic flux and quadrature axis current is responsible for the torque level.

Figure 12 presents the block diagram of the proposed speed control system using the indirect oriented field control strategy for the three-phase induction machine [39]. The system consists of an induction motor with a three-phase inverter, SVPWM modulation block, orientation block in which the rotor flux angle is calculated, block for the referential transformations (ABC to dq0) through Clarke and Park transformations, current control loop, speed control loop and position control loop. In this paper, only the design and tuning of the current and speed control loops will be addressed.

The equation of the dynamic model of the induction machine with indirect orientation presented in this paper is supported on the models and simplifications described in [5,39,40].

In an ideal field oriented of a three-phase induction machine, there is decoupling between the direct and quadrature axes, and the rotor flux is aligned to the direct axis (Figure 13). Thus, the flux and its derivative on the quadrature axis are null.

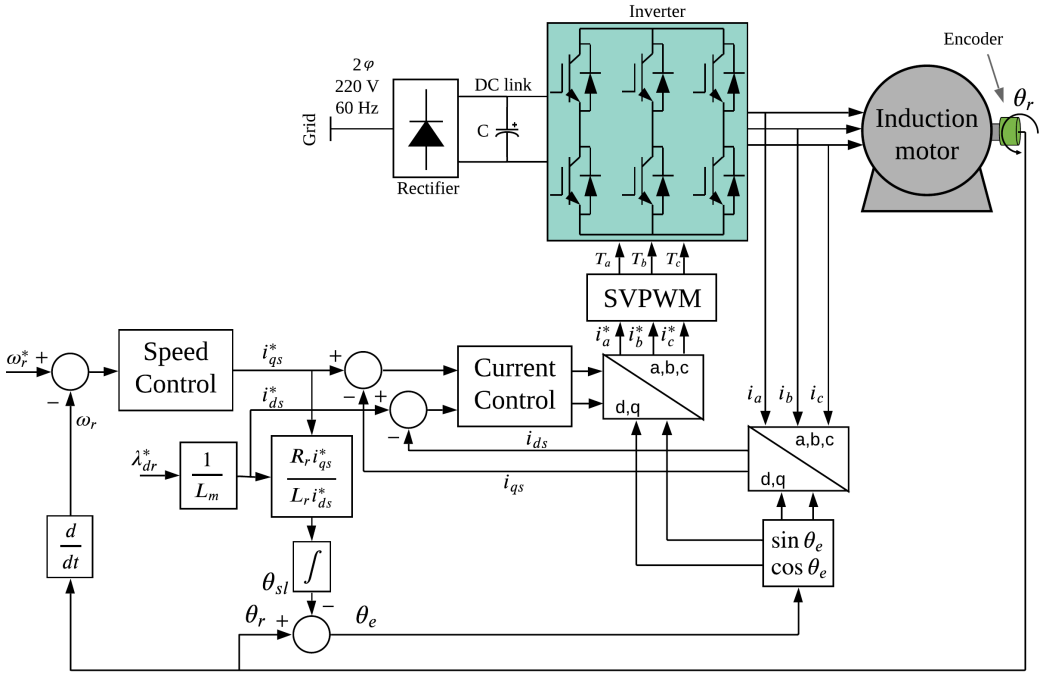

Figure 12. Indirect field oriented control scheme of induction machine.

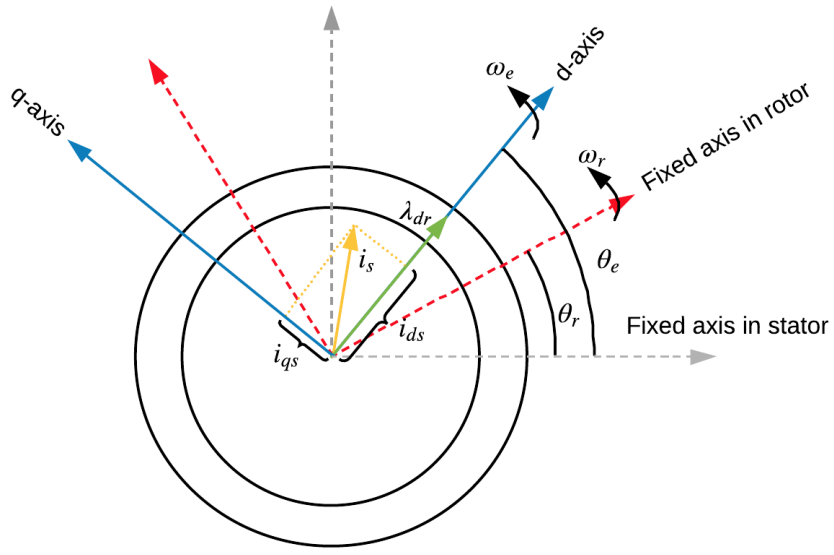

Figure 13. Analysis of the induction motor in the synchronous rotating referential.

Thus, the Equation (4) is used to calculate the rotor flux, given by

$$\lambda_{dr} = \frac{L_m i_{ds}}{1 + p\frac{L_r}{R_r}} \tag{4}$$

where L_m, L_r, R_r and i_{ds} represent mutual inductance, rotor inductance, rotor resistance, direct axis current, and p represents the derivative in time (d/dt), respectively.

The equation of the electromagnetic torque (Equation (5)) can be found considering that the electrical time constant of the system is negligible concerning the mechanical constant in the Equation (4), thus, it is obtained

$$T_e = \frac{3}{2}\frac{P}{2}\frac{L_m}{L_r} i_{qs} \lambda_{dr} \tag{5}$$

where T_e is the electromagnetic torque, P are the number of poles, λ_{dr} the direct axis flux and i_{qs} the quadrature axis current that denotes the torque command of the machine. The Equation (6) shows that the direct axis current is directly related to the magnetizing current of the machine, given by

$$i_{ds} = \frac{\lambda_{dr}}{L_m} \tag{6}$$

In the indirect field-oriented method, the frequency needs to be calculated in dq0 coordinates. Thus, the Equation (7), allows obtaining the slip frequency, given by

$$\omega_{sl} = \frac{L_m R_r i_{qs}^*}{L_r \lambda_{dr}} = \frac{R_r i_{qs}^*}{L_r i_{ds}^*} \tag{7}$$

The Equation (8) relates the torque, rotor velocity and angular position, given by

$$\theta_r = p\omega_r = \frac{1/J}{p + B/J}(T_e(p) - T_c(p)) \tag{8}$$

where θ_r, J, B and T_c denote the rotor position, moment of inertia, viscous coefficient of friction and load torque, respectively.

4. Space Vector Pulse Width Modulation—SVPWM

The SVPWM is a modulation technique that presents reduced switching number and allows better utilization of DC link voltage, compared to the SPWM (Sinusoidal Pulse Width Modutalion), widely used in scalar V/F AC drives. In addition, the SVPWM presents reduced current harmonic distortion and relatively simple digital implementation [3,41–43].

Figure 14 presents the waveforms of the eight possible states for a two-level three-phase inverter. Furthermore, it is considered that at the instant when the upper switch of one arm of the converter is closed, the lower one is open and reciprocal.

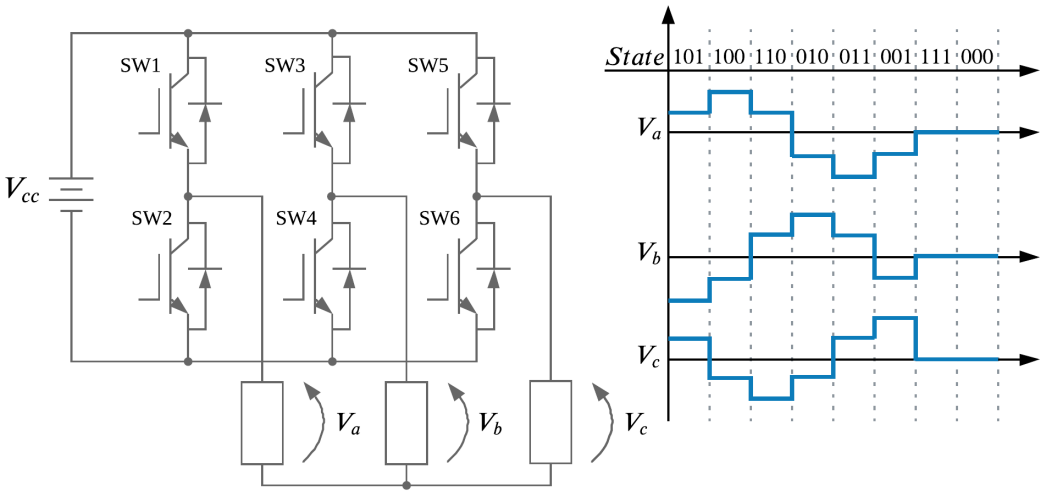

Figure 14. Single-phase voltage combinations for a two-level three-phase converter.

Each of the six nonzero states gives rise to a vector in the complex plane $\alpha\beta$ (Figure 15). The six active vectors have magnitude $2V_{cc}/3$ and lagged from each other by an angle of 60°. The null vectors are represented at the origin of the complex plane.

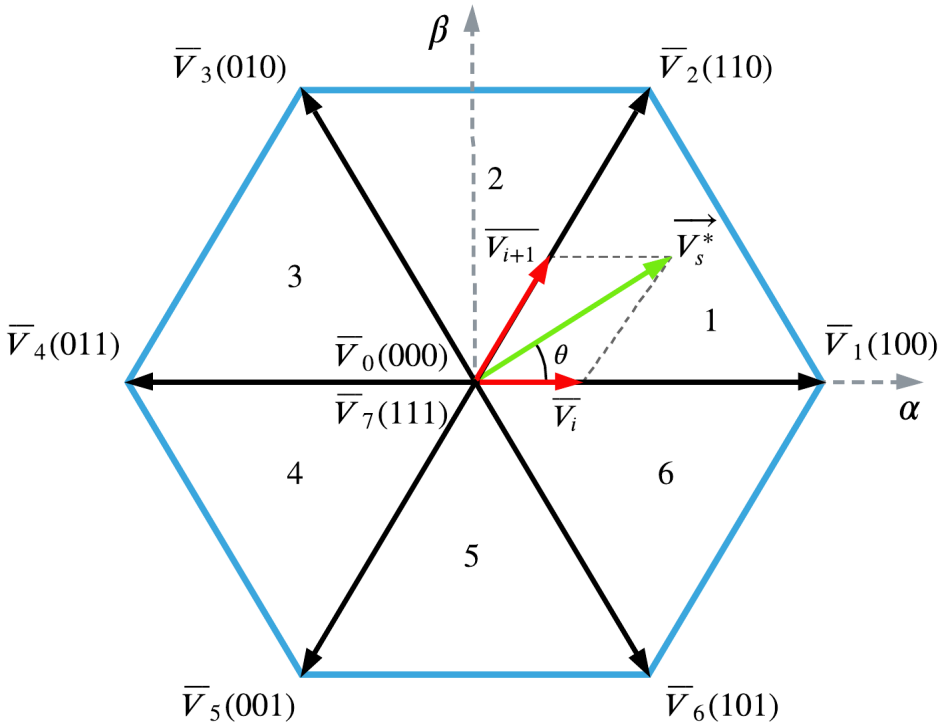

Figure 15. Hexagon of the converter output voltage spatial vectors.

To synthesize a reference voltage level ($\overline{V_s^*}$) during a sampling time interval (t_s) it is necessary to use adjacent voltage vectors and null vectors. The Equation (9) is used to calculate the reference voltage, given by

$$\overline{V_s^*} \cdot t_s = \overline{V_i} \cdot t_a + \overline{V_{i+1}} \cdot t_b + \overline{V_0} \cdot t_0 + \overline{V_7} \cdot t_7 \tag{9}$$

where $\overline{V_i}$ and $\overline{V_{i+1}}$ are adjacent vectors, $\overline{V_0}$ and $\overline{V_7}$ null vectors, t_a, t_b correspond to the length of time adjacent vectors are used, while t_0 and t_7 represent the duration of null vectors. The Equations (10)–(12) allow you to calculate the duration times of adjacent and null vectors, given by

$$t_a = \frac{\sqrt{3}\overline{V_s^*}}{V_{cc}} \cdot t_s \cdot sen(\frac{\pi}{3} - \theta) \tag{10}$$

$$t_b = \frac{\sqrt{3}\overline{V_s^*}}{V_{cc}} \cdot t_s \cdot sen(\theta) \tag{11}$$

$$t_0 = \frac{t_a + t_b - t_s}{2} \tag{12}$$

To avoid over-modulation in SVPWM modulation, the amplitude of the reference vector cannot be larger than the magnitude of the largest circumscribed radius of the hexagon. In SPWM the use of the DC link voltage is restricted to $V_{cc}/\sqrt{3}$. In, SVPWM the maximum magnitude of the voltage reference is $V_{cc}/\sqrt{2}$, i.e., 15% increase in the utilization of the voltage available on the DC link [44,45].

5. Controller's Tuning

Numerous types of speed controllers are available for induction motors. The Proportional Integral Derivative (PID) controller, which is widely utilized in industrial applications because of its simple design and structure [3].

To perform the tuning of the current and speed control loops, simplified linear representations of the system were used, which are based on the analysis and simplifications

described in [5,46]. The values of the gains of the PI controllers were initially determined by the root locus method in conformity with performance specifications and subsequently adjusted in the real system by an iterative approach to meet the required performance.

5.1. Current Control

In the design of the current loop controller the switching is considered perfect, so the reference voltage produced by the controller is exactly equal to the voltage applied to the machine terminals. The Equations (13) and (14) relate the reference voltages on the d and q axes of the controller with the currents that circulate through the windings of the machine, given by

$$v_{ds} = \underbrace{R_s i_{ds} + \sigma L_s \frac{d}{dt} i_{ds}}_{v'_{ds}} + \underbrace{\frac{L_m}{L_r} \frac{d}{dt} \lambda_{dr} - \omega_e \sigma L_s i_{qs}}_{v_{ds,ffd}} \tag{13}$$

$$v_{qs} = \underbrace{R_s i_{qs} + \sigma L_s \frac{d}{dt} i_{qs}}_{v'_{qs}} + \underbrace{\omega_e \frac{L_m}{L_r} \lambda_{dr} + \omega_e \sigma L_s i_{ds}}_{v_{qs,ffq}} \tag{14}$$

where R_s, L_s, σ, i_{ds}, i_{qs}, ω_e, $v_{ds,ffd}$, $v_{qs,ffq}$ represent stator resistance, stator inductance, dispersion coefficient, direct axis current, squaring axis current, synchronous rotary reference system speed, direct axis feedforward compensation, and feedforward compensation of the squaring axis, respectively. Figure 16 shows the current control loop.

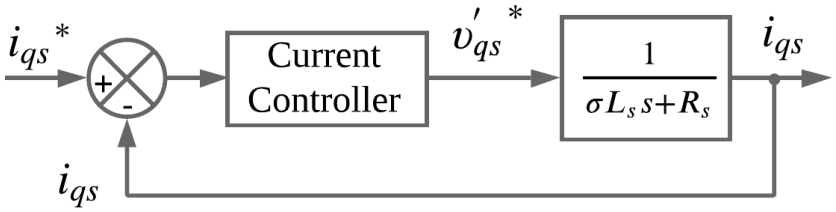

Figure 16. Current control loop diagram.

The voltage equations have coupling terms between them, in which the direct axis voltage depends on the quadrature axis current, and the quadrature axis voltage depends on the direct axis current. For control purposes, the compensation terms are considered disturbances and will therefore be disregarded for current controller design purposes. The reduced equations of the direct and quadrature axis voltages are given by Equations (15) and (16), assuming that the controller will be dominant enough to reject this error.

$$v'_{ds} = R_s i_{ds} + \sigma L_s \frac{d}{dt} i_{ds} \tag{15}$$

$$v'_{qs} = R_s i_{qs} + \sigma L_s \frac{d}{dt} i_{qs} \tag{16}$$

For the current loop controller design, the criteria presented in Table 4 were defined.

Table 4. Performance criteria for the current loops controllers (i_d and i_q).

Criteria	Value
Settling time (t_s)	0.008 s
Damping coefficient (ζ)	1.0
Overshoot (M_p)	0.0%

With the current loop model and performance criteria, the projected gains of the PI controller used in simulation environments and experimental tests are $K_p = 9.7158$ and $K_i = 4395$.

5.2. Speed Control

The mechanical model of the induction machine is linked to the electrical torque (T_e), load torque (T_c), the moment of inertia (J), mechanical velocity (ω_r) and viscous coefficient of friction, as shown in Equation (17)

$$\frac{d\omega_r}{dt} = \frac{1}{J}(T_e - B\omega_r - T_c) \tag{17}$$

Applying the Laplace transform in the Equation (17) and considering the load torque as an external disturbance, Equation (18) is obtained

$$p\Omega_r = \frac{1}{J}(T_e(p) - B\Omega_r(p)) \tag{18}$$

The quadrature axis current reference is provided from the PI speed controller, considering that the current control is perfect, and the reference current is reproduced in the machine windings, the speed controller model is presented in Figure 17, in which the relationship between the quadrature axis current and the electric torque is given by the machine's torque equation.

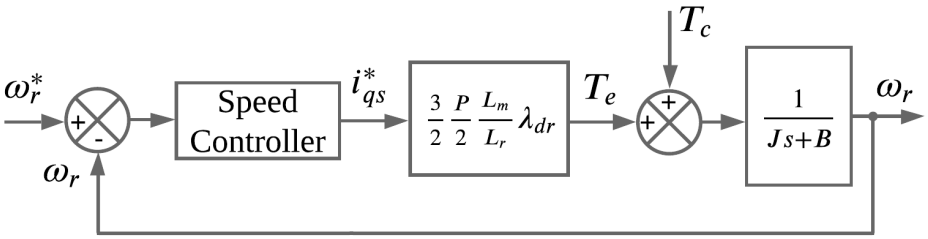

Figure 17. Speed control loop diagram.

For the speed loop controller design, the criteria presented in Table 5 were defined.

Table 5. Performance criteria for the speed loop controller.

Criteria	Value
Settling time (t_s)	0.4 s
Damping coefficient (ζ)	0.7
Overshoot (M_p)	20.0%

The projected gains of the speed loop controller used in simulation environments and experimental tests were $K_p = 0.0676$ and $K_i = 0.6939$.

6. Results

To analyze the behavior of control loops and vector control strategy, simulations were performed in the MATLAB/Simulink® software. Subsequently, the same tests were performed on the commissioned converter prototype. In this way, it is possible to examine the behavior of the converter both with regard to hardware operation and the practical implementation of the field-oriented control strategy on a real machine.

Initially, reference profiles were applied only to the direct axis current loop to evaluate the magnetization of the machine. Figure 18 presents the behavior of the direct axis loop for references of $i_d^* = 0.2$ A and $i_d^* = 0.4$ A. In addition, the bottom part shows the rotor speed of the machine.

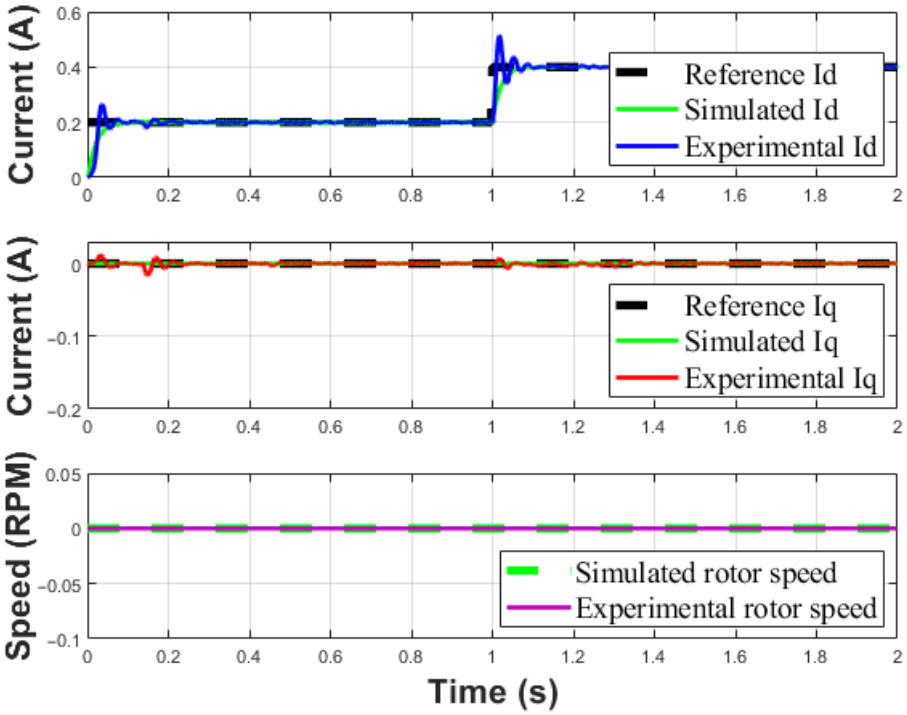

Figure 18. Current control loop behavior for i_d^* =0.2 A and $i_d^* = 0.4$ A.

It is verified in Figure 18 that the controller can keep the currents at the reference values. Furthermore, it is possible to analyze the behavior of the rotor speed, which due to the presence of only magnetizing current, the rotor stands still. Table 6 presents the performance results of the direct axis current controller.

Table 6. Direct axis current controller performance.

Criteria	Simulated Value	Experimental Value
Settling time (t_s)	0.06 s	0.07 s
Overshoot (M_p)	0.0%	27%

The overshoot present in the experimental i_d signal is related to simplifications adopted for the current controller design. The closed-loop transfer function of the current plant presents a zero. This zero was disregarded to calculate the PI controller gains. Thus, in the real system, this zero will cause a proportional overshoot for fast responses, but the settling time will be preserved.

To verify the behavior of the quadrature axis current controller, reference profiles were applied in positive step of 1.0 A and negative step of −1.0 A, as shown in Figures 19 and 20, respectively.

Analyzing the Figures 19 and 20, the controller can maintain the imposed references. Still, it is possible to highlight that for positive current values in the quadrature axis, the machine rotor rotates clockwise. However, for negative values of current in the quadrature axis, the machine rotation is reversed, characterized by negative speed values.

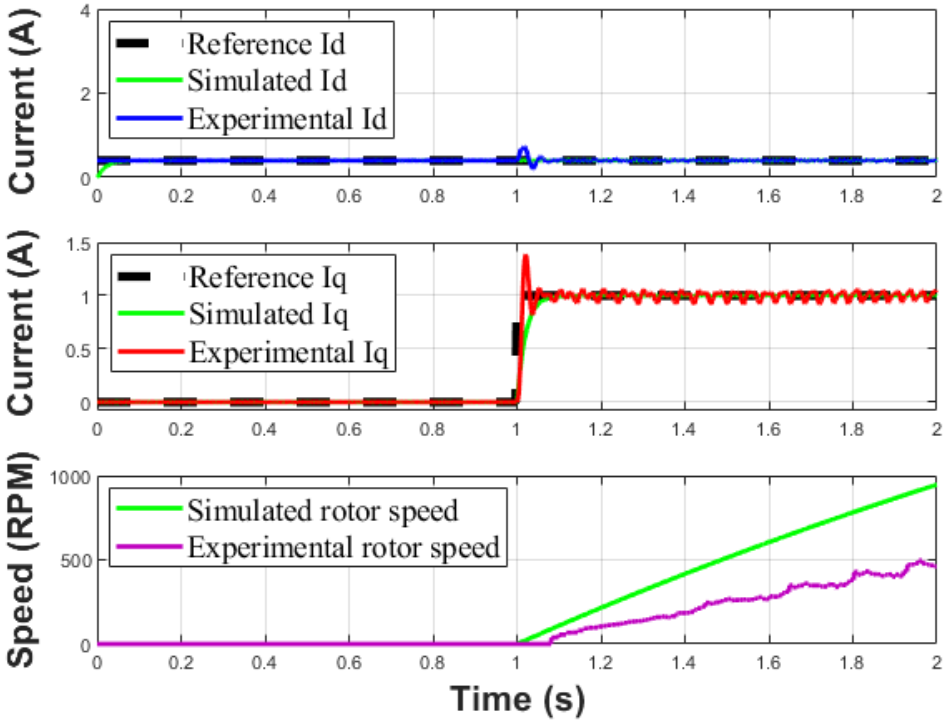

Figure 19. Current control loop behavior for $i_q^* = 1.0$ A.

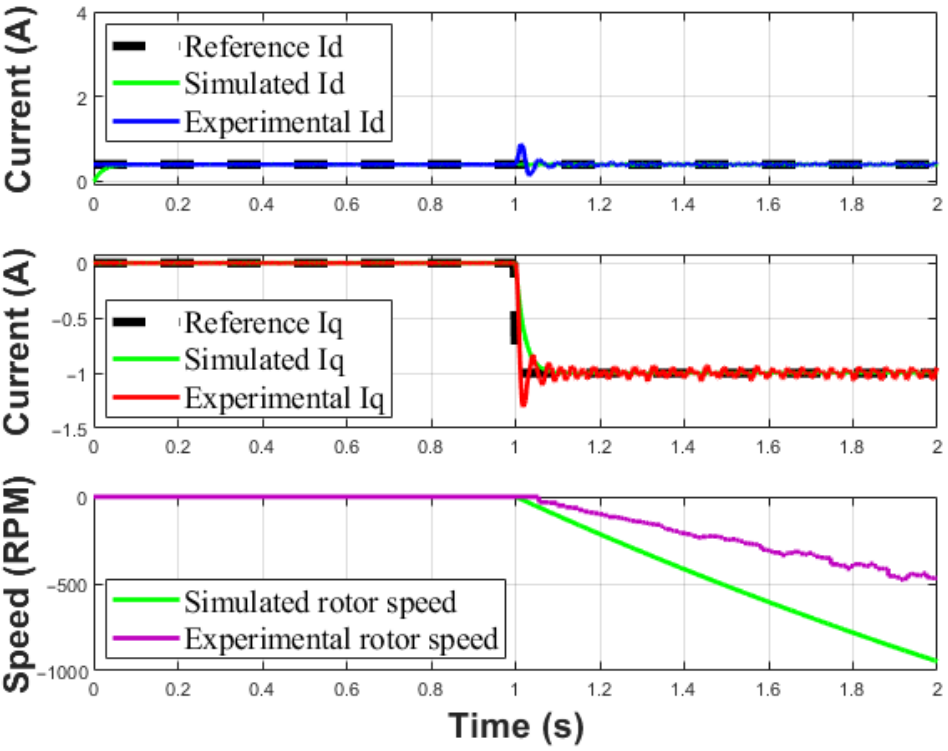

Figure 20. Current control loop behavior $i_q^* = -1.0$ A.

For both situations, the speed of the machine increases wildly, because there is no speed control loop. It is also noted that the speed of the machine in simulation assumes higher values than those collected in the experiments. The explanation for this is since in simulation many electrical and mechanical elements are considered ideal or even not present in the machine model. Thus, they do not contribute to the speed behavior of the

machine. In the same way as clarified for the current i_d, the overshoot of the current i_q control loop is justified.

Table 7 presents the performance parameters of the quadrature axis current controller.

Table 7. Controller performance for reference $i_q^* = 1.0$ A and $i_q^* = -1.0$ A.

Reference	Criteria	Simulated Value	Experimental Value
$i_q^* = 1.0$ A	Settling time (t_s)	0.05 s	0.05 s
	Overshoot (M_p)	0.0%	40%
$i_q^* = -1.0$ A	Settling time (t_s)	0.05 s	0.05 s
	Overshoot (M_p)	0.0%	40%

After validating the correct operation of the current control loop, the speed control loop controller was simulated and implemented in the digital signal processor. The direct axis current reference was set at a value of 0.4 A, which represents the magnetization of the machine, and experimentally was the value that presented the best speed and torque results. Tests were performed with step, trapezoidal, and sinusoidal references. For a positive step reference, initially with a reference of 300 RPM and then increasing to 500 RPM and returning to 300 RPM, as shown in Figure 21.

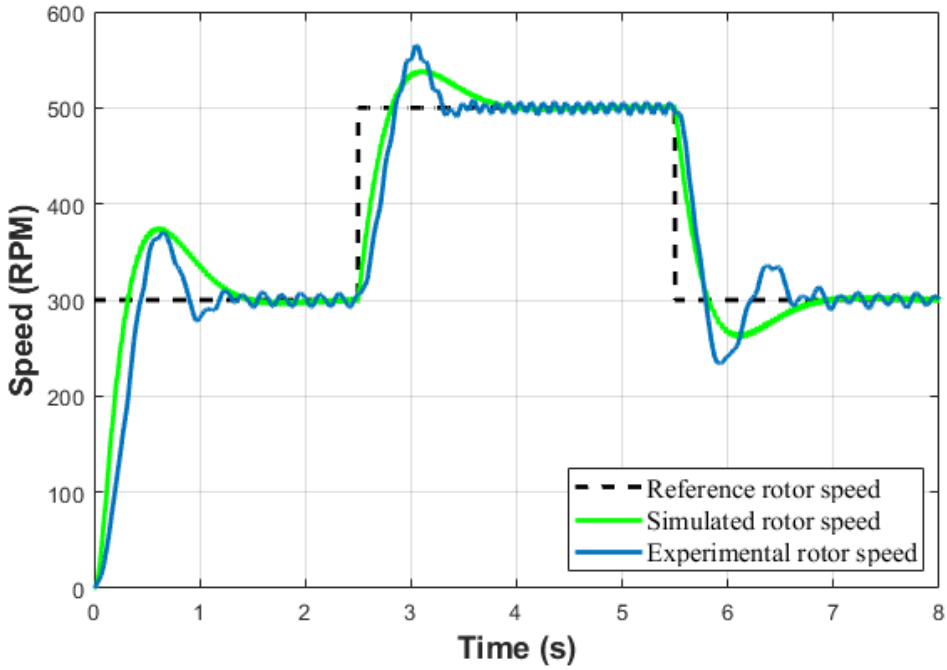

Figure 21. Behavior of the speed control loop with step reference.

Figure 22 shows the machine speed behavior for a trapezoidal reference, with a lower reference of 300 RPM and higher than 400 RPM.

Figure 23 shows the behavior of the machine speed for a sine reference with a frequency of 0.1 Hz and amplitude of 200 RPM.

Analyzing the results for the different speed references, it is evident the correct functioning of the implemented speed control loop. It is important to highlight that due to the accuracy of the encoder available during the tests, the speed signal has low amplitude oscillations. Table 8 presents the speed controller performance results for the three reference profiles.

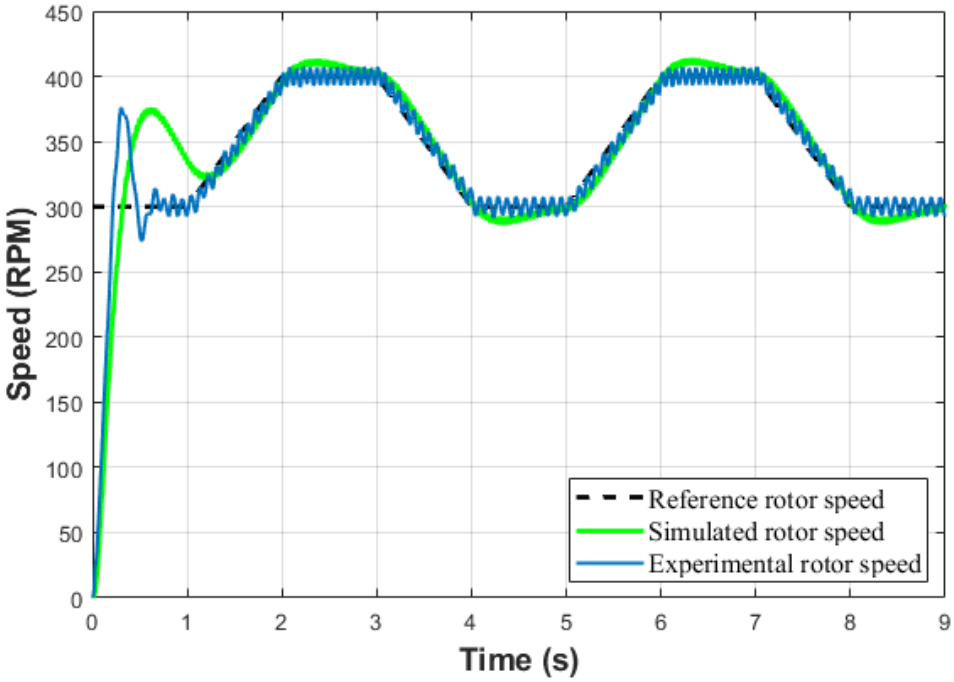

Figure 22. Behavior of the speed control loop with trapezoidal reference.

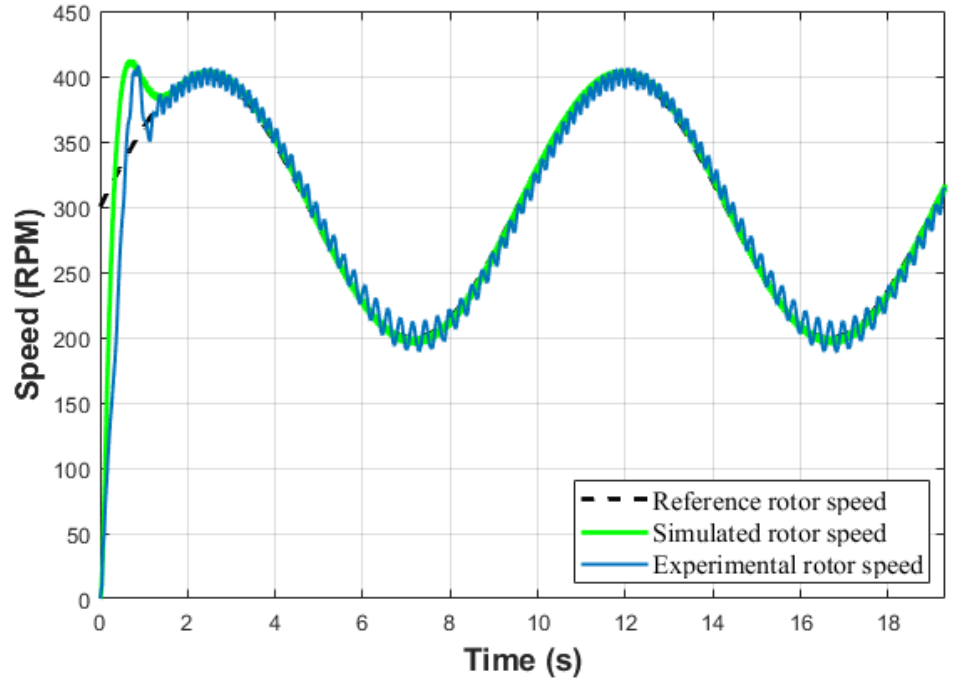

Figure 23. Behavior of the speed control loop with 0.1 Hz sinusoidal reference.

Table 8. Speed controller performance.

Reference	Criteria	Simulated Value	Experimental Value
Step	Settling time (t_s) Overshoot (M_p)	1.5 s 23%	1.2 s 33%
Trapezoidal	Settling time (t_s) Overshoot (M_p)	1.3 s 25%	0.7 s 26%
Sinusoidal	Settling time (t_s) Overshoot (M_p)	1.45 s 36%	1.3 s 35%

The overshoot signal for the speed loop with different speed profiles shows little difference from the performance specifications. The closed loop of the speed controller has a zero that was disregarded for the calculation of the controller gains. In the experimental environment, this zero contributes to the divergence of the peak speed from the simulated speed signal.

Due to the accuracy of the electrical parameters obtained through routine tests to make up the machine model, the dynamic performance of the current and speed controllers both in simulation and in the experimental tests did not rigidly follow the design specifications. In addition, simplifications in the current loop were adopted concerning the coupling terms that influence the actual behavior of the machine. However, the divergences present in the compliance with the performance criteria did not compromise the operation of the indirect field-oriented control strategy. The results presented validate the correct operation of the hardware, control loops and the implemented strategy.

7. Conclusions

The built AC drive presented results within the expected range. Thus, the methodology adopted for the commissioning of the power circuit and acquisition system met the intended goals. The use of the FNA41560 power module made the construction of the converter more versatile and economically viable, and it can be used for different drive applications for small induction machines.

The results show that both current and speed controllers presented similar results to the results obtained during the simulation step. To solve the divergences in performance, settling time and overshoot, verified in the tests, it is proposed to implement feedforward compensation in the current control loop. Furthermore, as the machine used is of small size, it is difficult to obtain electrical parameters with good accuracy only with conventional blocked-rotor and no-load tests.

Vector control allows you to control the torque and flux of the machine independently. However, this technique is dependent on the angle of the rotor flux and the fidelity of the machine's electrical and mechanical parameters. Thus, lines of research focus on approaches that use flux estimators or the use of controllers that are robust to parametric variations or adaptive or predictive type controllers.

SVPMW modulation proved to be an effective technique for driving the semiconductor switches of the IGBT bridge and relatively simplicity of implementation in the DSP. In addition, the use of this technique allows greater use of the voltage available on the DC link, reduced switching numbers and lower harmonic distortion in the machine line currents.

The developed test bench allows work focusing on other control strategies, activation of induction machines and PWM modulation techniques to be studied and validated.

Author Contributions: Conceptualization, R.R.G. and L.F.P.; methodology, R.R.G.; validation, R.R.G. and W.W.A.G.S.; writing—original draft preparation, R.R.G.; writing—review and editing, R.R.G., L.F.P. and W.W.A.G.S.; visualization, C.V.S., G.M.R. and F.F.R.; supervision, C.V.S., G.M.R. and F.F.R.; project administration, L.F.P. All authors have read and agreed to the published version of the manuscript.

Funding: This work has financial support from Federal University of Itajubá.

Institutional Review Board Statement: Not applicable.

Informed Consent Statement: Not applicable.

Data Availability Statement: The data presented in this study are available on request from the corresponding author.

Conflicts of Interest: The authors declare no conflict of interest.

References

1. Ustun, S.V.; Demirtas, M. Modeling and control of V/f controlled induction motor using genetic-ANFIS algorithm. *Energy Convers. Manag.* **2009**, *50*, 786–791. [CrossRef]
2. Reza, C.M.F.S.; Islam, M.D.; Mekhilef, S. A review of reliable and energy efficient direct torque controlled induction motor drives. *Renew. Sustain. Energy Rev.* **2014**, *37*, 919–932. [CrossRef]
3. Abd Ali, J.; Hannan, M.A.; Mohamed, A. A Novel Quantum-Behaved Lightning Search Algorithm Approach to Improve the Fuzzy Logic Speed Controller for an Induction Motor Drive. *Energies* **2015**, *8*, 13112–13136. [CrossRef]
4. Agamloh, E.; von Jouanne, A.; Yokochi, A. An Overview of Electric Machine Trends in Modern Electric Vehicles. *Machines* **2020**, *8*, 20. [CrossRef]
5. Novotny, D.W.; Lipo, T.A. *Vector Control and Dynamics of AC Drives*; Clarendon Press: Oxford, UK, 1996; ISBN 978-01-9856-439-3.
6. Morcos, M.M.; Lakshmikanth, A. DSP-based solutions for AC motor drives. *IEEE Power Eng. Rev.* **1999**, *19*, 57–59. [CrossRef]
7. Wai, R.-J.; Lin, K.-M. Robust decoupled control of direct field-oriented induction motor drive. *IEEE Trans. Ind. Electron.* **2005**, *52*, 837–854. [CrossRef]
8. Bim, E. *Máquinas Elétricas e Acionamento*, 4th ed.; Elsevier Editora Ltda: Rio de Janeiro, Brazil, 2018; ISBN 978-85-352-9067-7.
9. Zidani, F.; Nait-Said, M.-S.; Abdessemed, R.; Benoudjit, A. Induction machine performances in scalar and field oriented control. In Proceedings of the POWERCON'98. 1998 International Conference on Power System Technology, Beijing, China, 18–21 August 1998; Proceedings (Cat. No.98EX151); Volume 1, pp. 595–599.
10. Krein, P.T.; Disilvestro, F.; Kanellakopoulos, I.; Locker, J. Comparative analysis of scalar and vector control methods for induction motors. In Proceedings of the IEEE Power Electronics Specialist Conference—PESC '93, Seattle, WA, USA, 20–24 June 1993; pp. 1139–1145.
11. Finch, J.W. Scalar and vector: A simplified treatment of induction motor control performance. In Proceedings of the IEE Colloquium on Vector Control Revisited (Digest No. 1998/199), London, UK, 23–23 February 1998; pp. 1–4.
12. Liu, H.; Zhou, Y.; Jiang, Y.; Liu, L.; Wang, T.; Zhong, B. Induction motor drive based on vector control for electric vehicles. In Proceedings of the 2005 International Conference on Electrical Machines and Systems, Nanjing, China, 27–29 September 2005; Volume 1, pp. 861–865.
13. de Santana, E.S.; Bim, E.; do Amaral, W.C. A Predictive Algorithm for Controlling Speed and Rotor Flux of Induction Motor. *IEEE Trans. Ind. Electron.* **2008**, *55*, 4398–4407. [CrossRef]
14. Chang, G.-W.; Espinosa-Perez, G.; Mendes, E.; Ortega, R. Tuning rules for the PI gains of field-oriented controllers of induction motors. *IEEE Trans. Ind. Electron.* **2000**, *47*, 592–602. [CrossRef]
15. Lai, C.-K.; Lai, H.-Y.; Tang, Y.-X.; Chang, E.-S. Field Programmable Gate Array-Based Linear Shaft Motor Drive System Design in Terms of the Trapezoidal Velocity Profile Consideration. *Machines* **2019**, *7*, 59. [CrossRef]
16. Cabrera, R.S.; de Leon Morales, J. Some results about the control and observation of induction motors. In Proceedings of the 1995 American Control Conference—ACC'95, Seattle, WA, USA, 21–23 June 1995, Volume 3, pp. 1633–1637.
17. Shah, V. Implementation of Sensorless Field Oriented Current Control of Induction Machine. In Proceedings of the 2017 IEEE International Conference on Computational Intelligence and Computing Research (ICCIC), Coimbatore, India, 14–16 December 2017; pp. 1–5.
18. Vukosavic, S.N.; Stojic, M.R. On-line tuning of the rotor time constant for vector-controlled induction motor in position control applications. *IEEE Trans. Ind. Electron.* **1993**, *40*, 130–138. [CrossRef]
19. Moreira, J.C.; Lipo, T.A. A new method for rotor time constant tuning in indirect field oriented control. *IEEE Trans. Power Electron.* **1993**, *8*, 626–631. [CrossRef]
20. Jeon, S.H.; Oh, K.K.; Choi, J.Y. Flux observer with online tuning of stator and rotor resistances for induction motors. *IEEE Trans. Ind. Electron.* **2002**, *49*, 653–664. [CrossRef]
21. Jansen, P.L.; Lorenz, R.D. A physically insightful approach to the design and accuracy assessment of flux observers for field oriented induction machine drives. *IEEE Trans. Ind. Appl.* **1994**, *30*, 101–110. [CrossRef]
22. Pinheiro, D.D.; Carati, E.G.; Del Sant, F.S.; da Costa, J.P.; Cardoso, R.; de Stein, C.M.P. Improved Sliding Mode and PLL Speed Estimators for Sensorless Vector Control of Induction Motors. In Proceedings of the 2018 13th IEEE International Conference on Industry Applications (INDUSCON), Sao Paulo, Brazil, 12–14 November 2018; pp. 1030–1037.
23. Correa, M.B.R.; Jacobina, C.B.; dos Santos, P.M.; dos Santos, E.C.; Lima, A.M.N. Sensorless IFOC for single-phase induction motor drive system. In Proceedings of the IEEE International Conference on Electric Machines and Drives, San Antonio, TX, USA, 15 May 2005; pp. 162–166.
24. Kumar, A.; Ramesh, T. MRAS speed estimator for speed sensorless IFOC of an induction motor drive using fuzzy logic controller. In Proceedings of the 2015 International Conference on Energy, Power and Environment: Towards Sustainable Growth (ICEPE), Shillong, India, 12–13 June 2015; pp. 1–6.
25. Texas Instruments. TMS320F2837xD Dual-Core Delfino Microcontrollers—Technical Reference Manual. Available online: https://www.ti.com/lit/ug/spruhm8h/spruhm8h.pdf (acessed on 5 February 2021).
26. Mutlag, A.H.; Mohamed, A.; Shareef, H. A Nature-Inspired Optimization-Based Optimum Fuzzy Logic Photovoltaic Inverter Controller Utilizing an eZdsp F28335 Board. *Energies* **2016**, *9*, 120. [CrossRef]
27. Joy, P. Development of Software Using TMS320F28379D DSP. *Int. J. Res. Eng. Sci. Manag.* **2020**, *3*, 383–388.

28. Aravena, J.; Carrasco, D.; Diaz, M.; Uriarte, M.; Rojas, F.; Cardenas, R.; Travieso, J.C. Design and Implementation of a Low-Cost Real-Time Control Platform for Power Electronics Applications. *Energies* **2020**, *13*, 1527. [CrossRef]
29. Hart, D.W.; Júnior, A.P.; Abdo, R. *Power Electronics*, 1st ed.; The McGraw-Hill Companies: New York, NY, USA, 2011; ISBN 978-00-7338-067-4.
30. Gomes, R.R.; Pugliese, L.F.; Silva, W.W.A.G. Projeto de Dispositivo de Hardware para Acionamento de Máquinas de Baixa Potência. In Proceedings of the 2021 14th IEEE International Conference on Industry Applications (INDUSCON), São Paulo, Brazil, 15–18 August 2021; pp. 598–605.
31. Fairchild Semiconductor. FNA41560/FNA41560B2 Motion SPM 45 Series. Available online: https://br.mouser.com/datasheet/2/308/1/FNA41560B2_D-2313479.pdf (accessed on 6 June 2021).
32. de Oliveira, A.S.; de Andrade, F.S. *Sistemas Embarcados: Hardware e Firmware na Prática*, 2nd ed.; Editora Érica: São Paulo, Brazil, 2009; ISBN 978-85-3650-105-5.
33. Fairchild Semiconductor. High Speed-10 MBit/s Logic Gate Optocouplers. Available online: https://br.mouser.com/datasheet/2/308/1/HCPL2631_D-2314281.pdf (accessed on 28 May 2021).
34. Fairchild Semiconductor. AN-9070 Smart Power Module Motion SPM—Products in SPM45H Packages. Available online: https://au.mouser.com/pdfdocs/AN9070.pdf (accessed on 25 April 2021).
35. LEM. Current Transducer LA 55-P. Available online: https://www.lem.com/sites/default/files/products_datasheets/la_55-p_e.pdf (accessed on 10 May 2021).
36. LEM. Voltage Transducer LV 20-P. Available online: https://media.digikey.com/pdf/data%20sheets/lem%20usa%20pdfs/lv%2020-p.pdf (accessed on 08 May 2021).
37. Seybold, J.; Bülau, A.; Fritz, K.-P.; Frank, A.; Scherjon, C.; Burghartz, J.; Zimmermann, A. Miniaturized Optical Encoder with Micro Structured Encoder Disc. *Appl. Sci.* **2019**, *9*, 452. [CrossRef]
38. Bose, B.K. *Modern Power Electronics and AC Drives*; Prentice Hall: Upper Saddle River, NJ, USA, 2001; ISBN 978-01-3016-743-9.
39. Liaw, C.M.; Lin, F.J.; Kung, Y.S. Design and implementation of a high performance induction motor servo drive. *IEE Proc. B Electr. Power Appl.* **1993**, *140*, 241–248. [CrossRef]
40. Bose, B.K. *Power Electronics and Ac Drives*, 1st ed.; Prentice-Hall: Englewood Cliffs, NJ, USA, 1986; ISBN 978-01-3686-882-8.
41. Fang, H.; Feng, X.; Song, W.; Ge, X.; Ding, R. Relationship between two-level space-vector pulse-width modulation and carrier-based pulse-width modulation in the over-modulation region. *IET Power Electron.* **2014**, *7*, 189–199. [CrossRef]
42. Gopalakrishnan, K.S.; Narayanan, G. Space vector based modulation scheme for reducing capacitor RMS current in three-level diode-clamped inverter. *Electr. Power Syst. Res.* **2014**, *117*, 1–13. [CrossRef]
43. Zhang, Y.; Zhao, Z.; Zhu, J. A Hybrid PWM Applied to High-Power Three-Level Inverter-Fed Induction-Motor Drives. *IEEE Trans. Ind. Electron.* **2011**, *58*, 3409–3420. [CrossRef]
44. Tiwari, S.; Sahu, S.K. Space vector pulse width modulation based two level inverter. *Res. J. Eng. Sci.* **2017**, *6*, 8–12.
45. Kumar, N.; Jahangir, A.; Hoque, I. Modeling of Stand-Alone Three-phase Inverter for Various Loads using Space Vector Pulse Width Modulation. In Proceedings of the 2017 14th IEEE India Council International Conference (INDICON), Roorkee, India, 15–17 December 2017; pp. 1–6.
46. Mohan, N.; Undeland, T.M.; Robbins, W.P. *Power Electronics: Converters, Applications, and Design*, 3rd ed.; John Wiley & Sons: Hoboken, NJ, USA, 2003; ISBN 978-81-2651-090-0.